

## Journal Name

## ARTICLE TYPE

Cite this: DOI: 00.0000/xxxxxxxxxx

## Combinatorial neutron imaging method for hydrogenation catalysts

Marin Nikolic,<sup>\*,a,b,‡</sup> Filippo Longo,<sup>a,b</sup> Emanuel Billeter,<sup>a</sup> Alessia Cesarini,<sup>a,c</sup> Pavel Trtik,<sup>d</sup> and Andreas Borgschulte<sup>a</sup>

Received Date

Accepted Date

DOI: 00.0000/xxxxxxxxxx

Heterogeneous catalysts are materials with a complex structure on the atomic to mesoscopic scale, which depends on a variety of empirical parameters applied during preparation and processing. Although model systems clarified the general physical and chemical phenomena relevant to catalysis, such as hydrogen spillover, a rational design of heterogeneous catalysts is impeded by the sheer number of parameters. Combinatorial methods and high-throughput techniques have the potential of accelerating the development of optimal catalysts. We describe here a combinatorial approach based on hydrogen ad-/absorption and hydrogen–deuterium exchange quantified by neutron imaging. The method coined CONI is capable of measuring more than 50 samples simultaneously. As proof of concept, we study Pt catalyzed WO<sub>3</sub> as an archetypal spillover system, and Ni-catalyst supported on Al<sub>2</sub>O<sub>3</sub> and SiO<sub>2</sub>. CONI is ideally suited to distinguish between irreversible surface adsorption and reversible bulk absorption, providing quantitative information. Concretely, CONI yields the number of reversibly ad-/absorbed hydrogen atoms in and on a great number of various catalysts in a single experiment.

Received Date

Accepted Date

DOI: 00.0000/xxxxxxxxxx

Keywords: Combinatorial · Neutron Imaging · OH-Groups · OH-surface · hydrogen–deuterium exchange · H<sub>2</sub>-spillover Catalysis · Pressure gap · Reactor design · in-situ measurements

## 1 Introduction

Theoretical prediction and experimental testing of optimal catalyst structure, composition, and synthesis conditions, guided by chemical principles and knowledge of the literature, is elaborate and time consuming, because the parameter space to explore is vast. Combinatorial methods and high-throughput techniques have the potential of accelerating the process. These methods first developed for drug discovery involves compiling mixtures of a multitude of compounds into a library by parallel synthesis and

screening them for their properties.<sup>1–4</sup> The high-throughput approach relies on both high-throughput preparation as well analysis methods.<sup>5</sup> Thermographic infrared screening of combinatorial libraries of heterogeneous catalysts is one of the first examples of a highly parallel approach to catalyst screening, tracking the exothermic reactions that show up as hot spots. This thermal imaging technique provides convenient and rapid parallel screening of entire catalyst libraries, but no chemical information about the products generated, since only temperature is recorded.<sup>6</sup> To gain further insight into the products, Hui Su et al. developed a high-throughput screening method coupled with laser-induced fluorescence imaging that allows specific product formations to be tracked while a library of different catalysts is screened during the reaction.<sup>7–9</sup> Simultaneous analysis and screening under identical conditions not only shortens the time required, but also increases reproducibility and facilitates comparison of the performance of different samples, the latter two variables being important for catalyst development. This approach can be used to build a library of catalysts.

Our focus is on heterogeneous hydrogenation catalysis of CO<sub>2</sub>

<sup>a</sup> Laboratory for Advanced Analytical Technologies, Empa - Swiss Federal Laboratories for Material Science and Technology, Überlandstrasse 129, CH-8600 Dübendorf, Switzerland

<sup>b</sup> Department of Chemistry, University of Zürich, Winterthurerstrasse 190, CH-8057 Zürich, Switzerland

<sup>c</sup> Institute for Chemical and Bioengineering, Department of Chemistry and Applied Biosciences, ETH Zürich, Vladimir-Prelog-Weg 1-5/10, CH-8093 Zürich, Switzerland

<sup>d</sup> Laboratory for Neutron Scattering and Imaging, Paul-Scherrer-Institute, Forschungsstrasse 111, CH-5232 Villigen, Switzerland

† Electronic Supplementary Information (ESI) available: [details of any supplementary information available should be included here]. See DOI: 00.0000/00000000.

‡ E-mail: marin.nikolic@empa.ch

This document is the accepted manuscript version of the following article:

Nikolic, M., Longo, F., Billeter, E., Cesarini, A., Trtik, P., & Borgschulte, A.

(2022). Combinatorial neutron imaging methods for hydrogenation catalysts.

Physical Chemistry Chemical Physics. <https://doi.org/10.1039/D2CP03863C>

Journal Name, [year], [vol.], 1–12 | 1

to synthetic fuels such as methane or methanol in the context of the power-to-X concept.<sup>10–13</sup> Large scale renewable drop-in fuel production reducing greenhouse gas emissions requires highly active catalysts with minimal metal loading.<sup>14,15</sup> Typical catalysts for this reaction are Ni and Cu nano-particles for methane<sup>16–18</sup> and methanol<sup>19–21</sup> synthesis, respectively, that are deposited on oxide supports such as alumina, silica and zeolites.<sup>22,23</sup> Hydrogen is not only the reactant of the desired reaction; it simultaneously changes the catalyst, promoting or inhibiting catalytic activity.<sup>24</sup> The modification of a catalytic system upon hydrogen exposure as typically measured by temperature programmed reduction<sup>25</sup> is described by the term reducibility.<sup>24</sup> Using model systems, Karim et al.<sup>26</sup> demonstrated the link between hydrogen chemisorption and hydrogen mobility with hydrogen spillover and the reducibility of the system. However, application of these methods on individual real-world samples is error prone, as the various experimental factors can hardly be perfectly reproduced.<sup>14,25</sup>

To specifically monitor the hydrogen species during the reaction, we took advantage of the large neutron scattering cross section of hydrogen<sup>27–29</sup> compared to other elements. In addition, neutrons are not subject to any optical selection rules, making them optimal for tracking reactions involving hydrogen or hydrogen-containing species.<sup>30</sup> Here, we demonstrate a high-throughput analysis method based on neutron imaging to study several hydrogenation catalysts under identical conditions.<sup>30–32</sup> To achieve this, a high-throughput aluminum reactor setup able to accommodate up to 69 samples was designed (Fig. 1). Aluminum was used as reactor material due to its property of being nearly transparent to neutrons.<sup>31,32</sup> Furthermore, this particular design allowed to reduce the pressure gap reported by previous methods, where ultra-high vacuum is required,<sup>26</sup> as the analysis could be performed at pressures up to 1.5 bar bringing the experiment conditions closer to those used industrially. Hydrogen uptake and spillover were investigated on 64 samples by pressure dependent uptake and hydrogen–deuterium exchange experiments respectively. These experiments provide insights into the bonding between hydrogen and the catalyst surface, whether it is present as absorbed hydrogen, mobile hydrogen or as pre-existing OH groups.

We showcase the method coined CONI (combinatorial neutron imaging) method along the investigation of reversible and irreversible hydrogen uptake in oxide supported hydrogenation catalysts.

## 2 Experimental

**Reactor construction** The CF100 aluminum flanges were purchased from Baruvac AG and processed into our reactor by our workshop. The reactor consisted of 69 sample holders (depth 12 mm, diameter 5.6 mm) drilled into the first flange (see Fig 1) and a gas inlet and outlet on the second flange (see Fig 2). The reactor was heated with a heating jacket equipped with heating cartridges ( $P = 800\text{ W}$ ). The thick aluminum walls and the powerful heating cartridges guaranteed a fast heat exchange and temperature regulation (see Fig. 2). Thermal insulation was maintained by wrapping the reactor with several layers of aluminum, since other insulating materials used normally would absorb too much

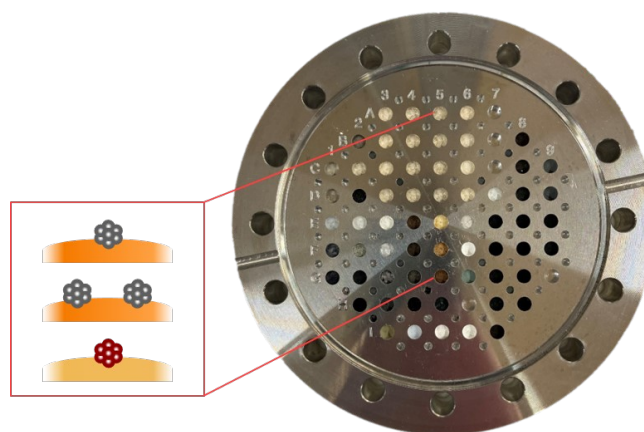


Fig. 1 Modified aluminum high-throughput reactor filled with various catalysts that differ in metal loading and metal-support combinations.

of the neutron beam.

**Reaction conditions and controlling** Gas flow and pressure were controlled with Bronkhorst thermal mass flow controllers and a backpressure regulator, connected to a Labview interface. The temperature was controlled with a temperature regulator from Eurotherm (see Fig 2 D). Typical flow rates were 100 sccm for  $\text{H}_2$  and  $\text{D}_2$ , pressures between 0 to 1.5 bar and temperatures from RT up to 350 °C.

**Catalyst preparation** All samples were prepared by the conventional wet impregnation method using metal nitrates. The samples were all ground and the powder was filled into the sample holes in the reactor.

$\text{Ni}(\text{NO}_3)_2 \cdot 6\text{H}_2\text{O}$  (Sigma Aldrich) in different loadings (0.5 %at, 5 %at, 40 %at) was added to  $\text{Al}_2\text{O}_3$  (Sigma Aldrich, 199443) and dissolved in deionized water. The samples were sonicated in a waterbath (RT) for 20 minutes and afterwards dried in an oven at 100 °C overnight. Calcination of the samples was performed in a tubular oven at 400 °C with an air flux of 1 L/min for 4 hours.<sup>33</sup>

$\text{Ni}(\text{NO}_3)_2 \cdot 6\text{H}_2\text{O}$  (Sigma Aldrich) in different loadings (0.5 %at, 5 %at, 40 %at) was added to  $\text{SiO}_2$  fumed (Sigma Aldrich), dissolved in deionized water and left for two weeks to impregnate. The samples were then transferred into a bigger beaker with 150 mL of deionized water and stirred at 70 °C. Later the temperature of the heating plate was set to 250 °C and the samples were continuously stirred overnight. On the next day the samples were once again transferred into a smaller beaker with rinsing of the residual samples with deionized water and dried in an oven at 90 °C overnight. Calcination of the samples was performed in a tubular oven at 400 °C with an air flux of 1 L/min for 4 hours.<sup>34</sup>

The  $\text{Pt@WO}_3$  sample was prepared by stirring an aqueous solution of  $\text{Pt}(\text{NH}_3)_4(\text{NO}_3)_2$  (Sigma Aldrich) dissolved at 1 %wt Pt with respect to  $\text{WO}_3$  (Sigma Aldrich, purity > 99.9%) in deionized water at 110 °C for 1 hour. The remaining solid was dried overnight at 125 °C and calcined at 550 °C for 3 hours<sup>35</sup>

Table 1 Elemental compositions of the different catalysts measured by X-ray photoelectronspectroscopy.

Catalyst	XPS				HAXPES			
	metal (%)	oxygen (%)	support cation (%)	metal/cation	metal (%)	oxygen (%)	support cation (%)	metal/cation
Pt@WO <sub>3</sub>	1.26	73.94	24.80	0.05	1.10	66.99	31.91	0.03
Al <sub>2</sub> O <sub>3</sub>	-	66.89	33.11	-	-	56.41	43.59	-
Ni@Al <sub>2</sub> O <sub>3</sub> L	0.39	67.12	32.5	0.01	0.35	55.59	44.06	0.01
Ni@Al <sub>2</sub> O <sub>3</sub> M	7.95	66.12	25.92	0.31	4.71	57.72	37.57	0.13
Ni@Al <sub>2</sub> O <sub>3</sub> H	43.14	51.02	5.84	7.39	38.61	47.32	14.07	2.74
SiO <sub>2</sub>	-	69.55	30.45	-	-	61.67	38.33	-
Ni@SiO <sub>2</sub> L	0.07	69.67	30.27	0.002	0.18	62.22	37.60	0.005
Ni@SiO <sub>2</sub> M	0.84	69.10	30.06	0.03	0.87	62.19	36.94	0.02
Ni@SiO <sub>2</sub> H	2.88	68.68	28.44	0.10	3.12	61.23	35.65	0.09

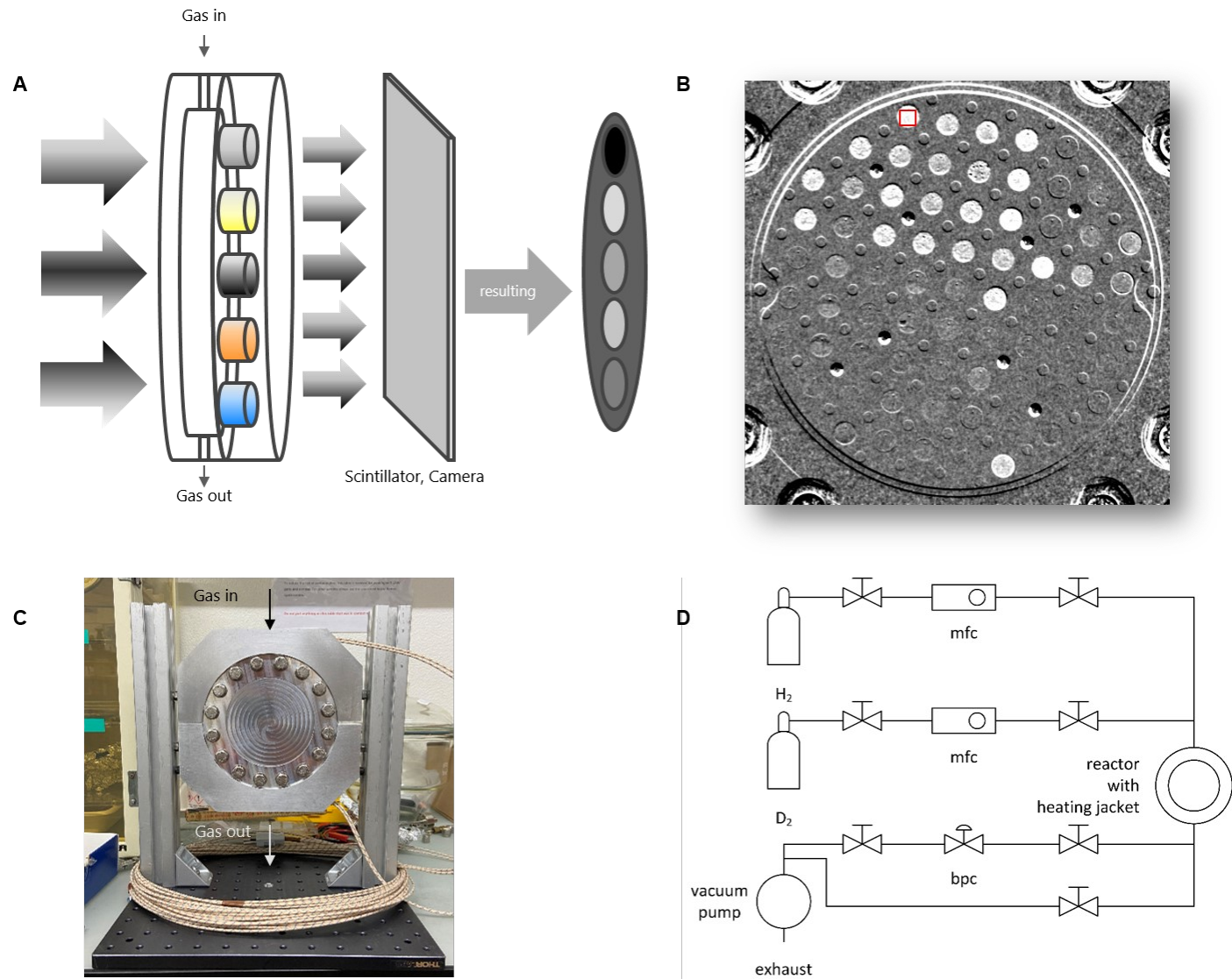


Fig. 2 A. Schematic representation of the neutron imaging process. The neutron beam irradiates the reactor filled with the samples and leaves with reduced intensity, which is detected by a scintillator, resulting in an area-resolved image. B. One Neutron image of the reactor during the experimental run, with a marked area corresponding to the area-averaged intensity used for  $I_{ij}$  in red. C. Photograph of the reactor with heating jacket, heating cartridges and reactor holder. D. Schematic representation of the experimental setup.

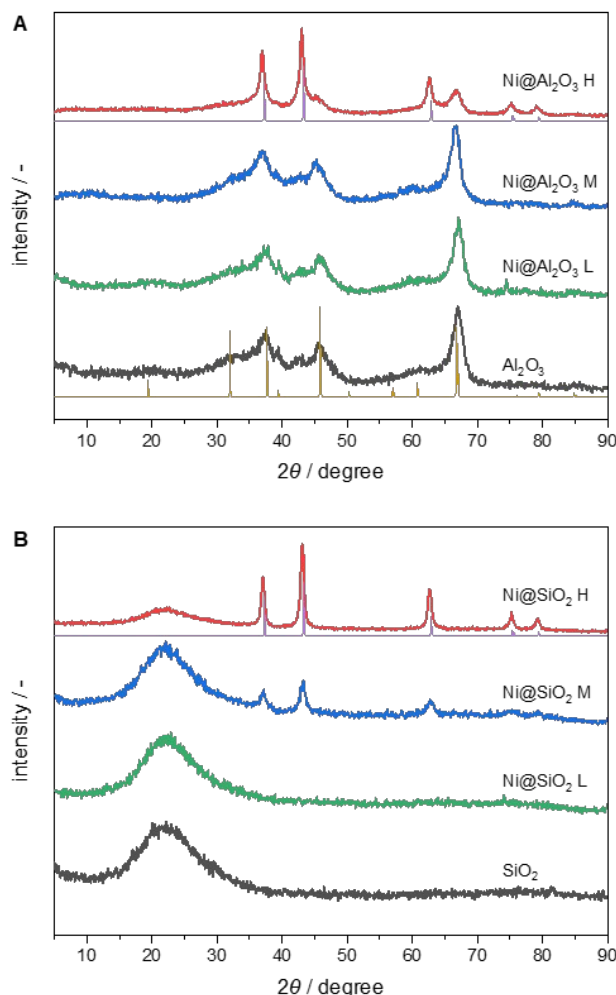


Fig. 3 X-ray diffraction pattern of the nickel catalysts on  $\text{Al}_2\text{O}_3$  (A.) and  $\text{SiO}_2$  (B.) compared to reference patterns of  $\gamma\text{-Al}_2\text{O}_3$  (ICSD number 66559, in yellow color) and  $\text{NiO}$  (ICSD number 9866, in purple color).

**Catalyst characterization** Catalysts characterization was performed by powder X-ray diffraction (XRD), X-ray photoelectron spectroscopy (XPS & HAXPES) and surface area measurements by  $\text{N}_2$  adsorption at 77 K using the Brunauer, Emmett and Teller (BET) analysis.

X-ray photoelectron spectroscopy (XPS) was combined with hard X-ray photoelectron spectroscopy (HAXPES) using a PHIQuantes spectrometer (Ulvac-Phi), equipped with a conventional low-energy  $\text{Al-K}\alpha$  source (1486.6 eV) and a high energy  $\text{Cr-K}\alpha$  (5414.7 eV) X-ray source. Both sources are high flux focused monochromatic X-ray beams (further details below). The methods give the elemental concentration of the catalyst (Table 1) with an averaged information depth of 2–4 nm and 10–20 nm for the  $\text{Al-}$  and  $\text{Cr-}$  source, respectively.<sup>36</sup> A comparison of the two concentrations reveals the distribution of the elements as expressed by the ratio between the catalytic metal and the support cation ( $\text{W}^{6+}$ ,  $\text{Al}^{3+}$ ,  $\text{Si}^{4+}$ ). As an example, the sample  $\text{Ni@Al}_2\text{O}_3$  H with

Table 2 Surface area and pore volume of the catalysts.

Catalyst	BET surface area ( $\text{m}^2 \text{g}^{-1}$ )	pore volume ( $\text{cm}^3 \text{g}^{-1}$ )
$\text{Pt@WO}_3$	3.49	0.042
$\text{Al}_2\text{O}_3$	179.87	0.280
$\text{Ni@Al}_2\text{O}_3$ L	180.03	0.285
$\text{Ni@Al}_2\text{O}_3$ M	180.34	0.276
$\text{Ni@Al}_2\text{O}_3$ H	139.41	0.219
$\text{SiO}_2$	349.35	0.837
$\text{Ni@SiO}_2$ L	249.22	0.985
$\text{Ni@SiO}_2$ M	249.02	0.976
$\text{Ni@SiO}_2$ H	173.10	0.971

highest Ni-loading contains 43 % at Ni within a depth of around 3 nm, but only 39 % at within 15 nm.<sup>37</sup> The metal-cation ratio changes from 7.4 to 2.7. This means that Ni is concentrated at the surface in the oxidized form. The trend is observed for all investigated systems (Table 1).

XPS/HAXPES detail spectra: A detection angle of  $\theta = 45^\circ$  with respect to the sample surface was used. XPS detail spectra were recorded with a step size of 0.05 eV at a constant pass energy of 55 eV averaging 10 scans using the  $\text{Al-K}\alpha$  source (power 24.5 W; beam diameter 100  $\mu\text{m}$ ). HAXPES detail spectra were recorded with a step size of 0.05 eV at a constant pass energy of 55 eV averaging 80 scans using the  $\text{Cr-K}\alpha$  (power 51.6 W; beam diameter 91.6  $\mu\text{m}$ ). Quantification of each element was performed using the MultiPak 9.9 software of Ulvac-Phi. Atomic concentration of the elements were calculated from the integrated peak areas, using the sensitivity factors provided by the manufacturer, as derived according to ISO 18118.

X-ray diffraction (XRD) patterns were obtained using a PANalytical X'Pert-Pro powder X-ray diffractometer, using  $\text{Cu K}\alpha$  monochromatized radiation (1.541 Å) in the range of  $2\theta = 5\text{--}90^\circ$  (X-ray gun setting at 45 kV and 40 mA).

Although  $\text{Al}_2\text{O}_3$  and  $\text{SiO}_2$  are nanocrystalline and amorphous materials, respectively, XRD gives some important background information (Fig. 3).  $\text{Al}_2\text{O}_3$  is identified by broad peaks;  $\text{SiO}_2$  is visible through a broad amorphous background at lower scattering angles. The background shape does not change with catalysts loading, indicative of an unmodified support after Ni-loading. On  $\text{Al}_2\text{O}_3$ , peaks of  $\text{NiO}$  are visible for highest Ni-concentrations only, while the corresponding peaks occur for much lower Ni-concentrations on  $\text{SiO}_2$ . This indicates that Ni is finer dispersed on  $\text{Al}_2\text{O}_3$  and  $\text{SiO}_2$  during the impregnation/calcination process, i.e.,  $\text{NiO}$  agglomerates faster on  $\text{SiO}_2$  to XRD-visible particles ( $d > 14$  nm) than on  $\text{Al}_2\text{O}_3$ . Nucleation of nanoparticles relies on the existence anchor points (seeding),<sup>38,39</sup> mostly defects, which are different on both supports.

$\text{N}_2$  sorption at 77 K was measured in a Micromeritics TriStar II analyzer. Samples (approximately 0.05 g) were evacuated to 50 mbar at 623 K for 12 h prior to the measurement. The Brunauer–Emmett–Teller (BET) method was applied to calculate the total surface area, SBET. The pore volume,  $V_{\text{pore}}$ , was determined from the amount of  $\text{N}_2$  adsorbed at a relative pressure of  $p/p_0 = 0.99$ . The surface area of the impregnated catalysts decreases with increasing nickel concentration (Table 2). The same

trend is observed for the total pore volume, but less pronounced especially between catalysts with similar nickel loading.

**Neutron imaging** The reactor was placed in a collimated neutron beam (thermal neutrons) in the NEUTRA<sup>40</sup> radiography station (SINQ, PSI Switzerland)<sup>41</sup> in front of a detector, a scintillator CCD-camera system. The scintillator, doped with gadolinium (neutron absorber), converts the neutron beam into visible light, which is then recorded by the CCD-camera via a mirror.

The neutrons are markedly scattered by hydrogen only, while aluminum has a relatively small effective cross section for neutrons.<sup>27,28</sup> Images of the ongoing reaction are taken every 20 seconds, allowing *in-situ* analysis of processes on a minute timescale.

**Processing of neutron images** Image and data processing were performed with *ImageJ* software using built-in functions and a *Matlab* script for the data extraction and calculation of the neutron attenuation  $A$  in  $\text{cm}^{-1}$  and hydrogen concentration  $c$  in  $\text{mol cm}^{-3}$ :

$$c = \frac{A}{\mu N_A} = -\frac{\ln\left(\frac{I_{ij}-I_{DC}}{I_{0j}-I_{DC}}\right)}{d\mu N_A} \quad (1)$$

with  $d$  being the sample thickness (here 1.2 cm),  $N_A$  the Avogadro constant,  $\mu = 4.7 \cdot 10^{-23} \text{ cm}^2$  the scattering cross-section of neutrons for hydrogen in water molecules by the thermal neutrons of NEUTRA<sup>42</sup> (see discussion),  $I_{ij}$  is the extracted area-averaged intensity of each image measured for 20 seconds, with  $i$  indicating the image number from the experimental sequence and  $j$  representing the sample,  $I_{DC}$  the background noise (no neutron flux) from the CCD camera and  $I_{0j}$  being the reference image of each experimental run, which is derived from the mean value of several images measured under *vacuum* at the beginning of each experimental sequence.

Before data extraction from the images, the raw data images were processed to correct inhomogeneities of the experimental setup. First, the background noise from the CCD camera  $I_{DC}$  was subtracted from each image  $I_{ij}$ . Second, outliers caused by direct hits of  $\gamma$ -photons on the CCD camera were removed using the "remove outliers" option in *Image J* (pixels 4.0, threshold 300) for all acquired images. In a next step the images were corrected for scattered neutrons by black-body correction using the *Kip-tool* software.<sup>43</sup> The black body correction is required for neutron imaging analysis, because no optical elements are included for neutron imaging leading to artifacts from multi-scattering and secondary radiation. It is particularly important for samples with highly different scattering areas as is the case for the multi-sample reactor.<sup>43</sup>

Since we are only interested in the difference in hydrogen uptake of the samples, the images were normalized by the reference image  $I_{0j}$ . All corrections (except the black-body corrections) were performed with the software *Image J*. The data was extracted using a *Matlab* script extracting the now corrected, area-averaged intensities (indicated by a red square in Fig. 2B) of each sample for each experimental run.

### 3 Methodology

Before each sequence, the reactor was degassed at 350°C in *vacuum* for at least 30 min for all measurement series. The vacuum pressure was given by the rotary pump base pressure of around 0.1 mbar. Then the reactor was set to the desired temperature of the experiment. The first 5-10 images (100-200 s) of the reactor in *vacuum* were later used as reference image  $I_{0j}$  for normalization. Hydrogen was then added to the samples at a flow rate of 100 sccm and the pressure was increased stepwise from 0.5 to 1.5 bar. After this step, vacuum was again applied to monitor the reversibility of the hydrogen uptake. This was followed by the steady-state isotopic transient kinetic analysis, in which hydrogen was alternately exchanged with deuterium and vice versa (flow rates 100 sccm at 1 bar).

The difficulty of hydrogen analysis in catalysts stems from two facts: the coverage of mobile hydrogen, e.g., reversibly adsorbed hydrogen on the surface of the catalyst is high at high pressures and low in *vacuum* ( $\theta = 1 \rightarrow 0$ ).<sup>44</sup> The number of irreversibly adsorbed hydrogen atoms, e.g., hydrogen bound to the surface as hydroxide can be high, too.<sup>45</sup> However, the averaged hydrogen concentration as determined by non-local measurements is orders of magnitude lower than the local surface concentration. Hydrogen is also dissolved in the bulk at low concentrations by practically every material,<sup>46</sup> which makes the assignment difficult. The second difficulty is that hydrogen can be detected and quantified by very few *in-situ* methods only.<sup>47-49</sup> Terreni et al.<sup>32,50</sup> demonstrated the use of neutron radiography for hydrogen detection in catalysts. Neutron imaging is element-specific for hydrogen and compatible with the harsh conditions in catalysis, but lacks chemical selectivity. To have some chemical information, the experimental procedure is adapted by the parallel measurement (high-throughput) of designed model samples. A multitude of samples is prepared in a way that changes in the hydrogen uptake can be traced back to the intentional structural or chemical differences of the samples (combinatorial approach).

The averaged hydrogen concentration  $c$  is obtained by attenuation of neutrons by scattering, see experimental section, utilizing the Lambert-Beer law (eq. 1). The attenuation of neutrons depends on a variety of parameters including total number of neutrons, detection efficiency, scattering by reactor walls and scattering by the atoms of the sample including the irreversibly adsorbed hydrogen. The number of irreversibly adsorbed hydrogens atoms (mostly as OH) will not vary upon change of the conditions applied here (hydrogen pressure, temperature), unless very extreme conditions are applied, which are inaccessible in most setups.<sup>51</sup> As the attenuation is derived from intensity changes, irreversibly absorbed hydrogen cannot be detected. To account for these hydrogen atoms, the samples are exposed to deuterium, which can exchange with the hydrogen already present in the samples. The exchange process is a chemical reaction with a negligible change of the Gibbs free energy,<sup>52</sup> and thus mainly kinetically limited.<sup>53</sup> Deuterium has a markedly lower neutron scattering cross section.<sup>28</sup> The attenuation of neutrons by a sample containing both reversible and irreversibly absorbed hydrogen decreases upon exposure to deuterium proportional to the total amount of H.

With these two methods, we can access the kinetics as well as thermodynamics of hydrogen sorption in catalyst. The dependence of these properties on the microstructure is probed by studying a series of samples with identical setup but one structural parameter. In this paper, we showcase this idea along  $\text{Al}_2\text{O}_3$  and  $\text{SiO}_2$  supported Ni catalysts with various amounts of Ni corresponding to a different coverage of the oxide by the Ni metal particles. A limited chemical selectivity is obtained by studying a series of identical samples, in which one constituent is varied. Here, we use various supports as an example.

## 4 Results

In the experiment, 64 different samples were measured simultaneously under exactly the same reaction conditions. We first start with a sample couple interacting contrarily with hydrogen:  $\text{Pt@WO}_3$  and  $\text{Ni@Al}_2\text{O}_3 \text{ H}$ .  $\text{WO}_3$  is the archetypal oxide known to absorb reversibly up to one hydrogen per formula unit.<sup>48,54,55</sup> In addition to the reversibly absorbed bulk hydrogen,  $\text{WO}_3$  has some irreversible hydroxide and/or water adsorbed at the surface.<sup>48,56</sup> Hydrogen in and on  $\text{Al}_2\text{O}_3$  is a complex chemical system. Due to the high stability of  $\text{Al}_2\text{O}_3$ ,<sup>57</sup> hydrogen in  $\text{Al}_2\text{O}_3$  is limited to defects in the material.<sup>58</sup> Only at high water partial pressure, hydroxide formation is thermodynamically favored.<sup>59</sup> The situation is different at the surface. Since long, the rich surface chemistry of  $\text{Al}_2\text{O}_3$  is investigated and utilized for catalysis applications.<sup>51</sup>  $\text{H}_2$  readily chemisorbs on the pristine  $\text{Al}_2\text{O}_3$  surface forming Al-H and O-H. The number and reactivity depends sensitively on the water partial pressure.<sup>60</sup> Technical surfaces are usually hydroxylated, and heating up to 500 °C leads only to a partial dehydroxylation.<sup>60</sup> Nevertheless, hydrogen–deuterium exchange takes place on such surfaces.<sup>60,61</sup> In both cases, the metal nano-particles of Pt on  $\text{WO}_3$  and Ni on  $\text{Al}_2\text{O}_3$ , respectively, are added to accelerate hydrogen dissociation. Their influence is discussed later.

Figure 4 shows the neutron attenuation  $\frac{\ln(I/I_0)}{d}$  from  $\text{Ni@Al}_2\text{O}_3 \text{ H}$  and  $\text{Pt@WO}_3$  during a typical measurement cycle (see Sec. 2 for details). After annealing in *vacuum*, all samples are simultaneously exposed to hydrogen at 0.5 bar and subsequently up to 1.5 bar. The attenuation of  $\text{Ni@Al}_2\text{O}_3 \text{ H}$  hardly changes. There is a small increase at the pressure step, which is attributed to hydrogen in the macro- and micro pores of the sample (red arrow in Fig. 4A). Applying vacuum has no significant effect (blue arrow in Fig. 4A). With exposure to deuterium, a strong positive signal develops indicative of irreversibly adsorbed H, which is exchanged by D (green arrow in Fig. 4A). Within the measurement time, saturation of the exchange is not reached.

An extrapolation gives a neutron attenuation of  $A = 0.04 \text{ cm}^{-1}$ . This translates into a total number of irreversibly absorbed hydrogen of

$$c = \frac{A}{\mu} \cdot \frac{V}{m_{\text{ABET}}} \simeq 5.2 \text{ H nm}^{-2} \quad (2)$$

with the mass  $m = 0.274 \text{ g}$  and volume  $V = 0.24 \text{ cm}^3$  of the sample and the measured surface area (see table 2). This is in good agreement with literature, if H is present as OH on the surface: Zhang et al.<sup>62</sup> find  $4 \text{ OH nm}^{-2}$  by MAS-NMR on  $\gamma$ -alumina.

The amount of absorbed hydrogen is significantly smaller (red

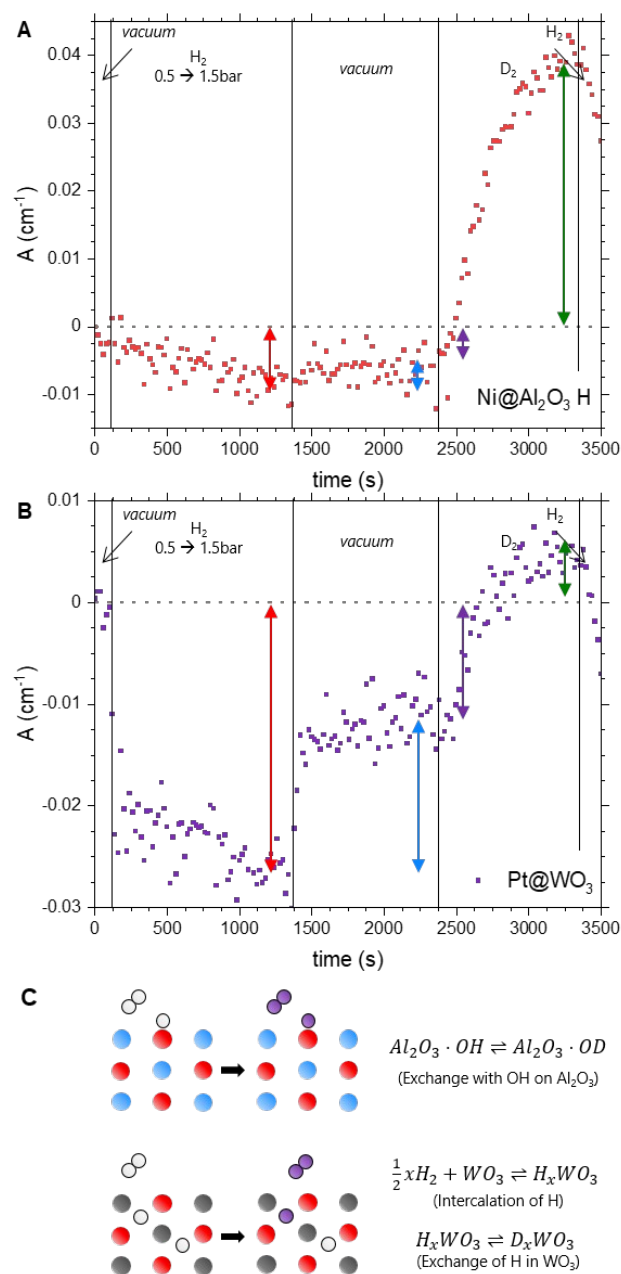


Fig. 4 A. and B. show the neutron attenuation in  $\text{cm}^{-1}$  versus time in s of the catalysts  $\text{Ni@Al}_2\text{O}_3 \text{ H}$  and  $\text{Pt@WO}_3$  at 200 °C. The arrows reflect the hydrogen uptake (red), hydrogen desorption (blue), exchange of mobile/intercalated hydrogen with deuterium (purple) and the exchange of the hydrogen with deuterium in the previously present hydroxy groups (green). C. Schematic representation of the hydrogen intercalation and the hydrogen–deuterium exchange in the two catalysts.

arrow in Fig. 4A). Within measurement time, we reach neutron attenuation for the pristine  $\text{Al}_2\text{O}_3$  support of  $A = 0.003 \text{ cm}^{-1}$  at 100 °C corresponding to a concentration of  $c = 0.3 \text{ H nm}^{-2}$ , at 200 °C a concentration of  $c = 0.5 \text{ H nm}^{-2}$  and a concentration of  $c = 2.1 \text{ H nm}^{-2}$  at 300 °C (Fig. 5). Jourbert et al. find  $c = 0.043 \text{ H nm}^{-2}$  and  $c = 0.069 \text{ H nm}^{-2}$  of Al-H sites at 25 °C and 150 °C, respectively using a titration procedure quantified by solid

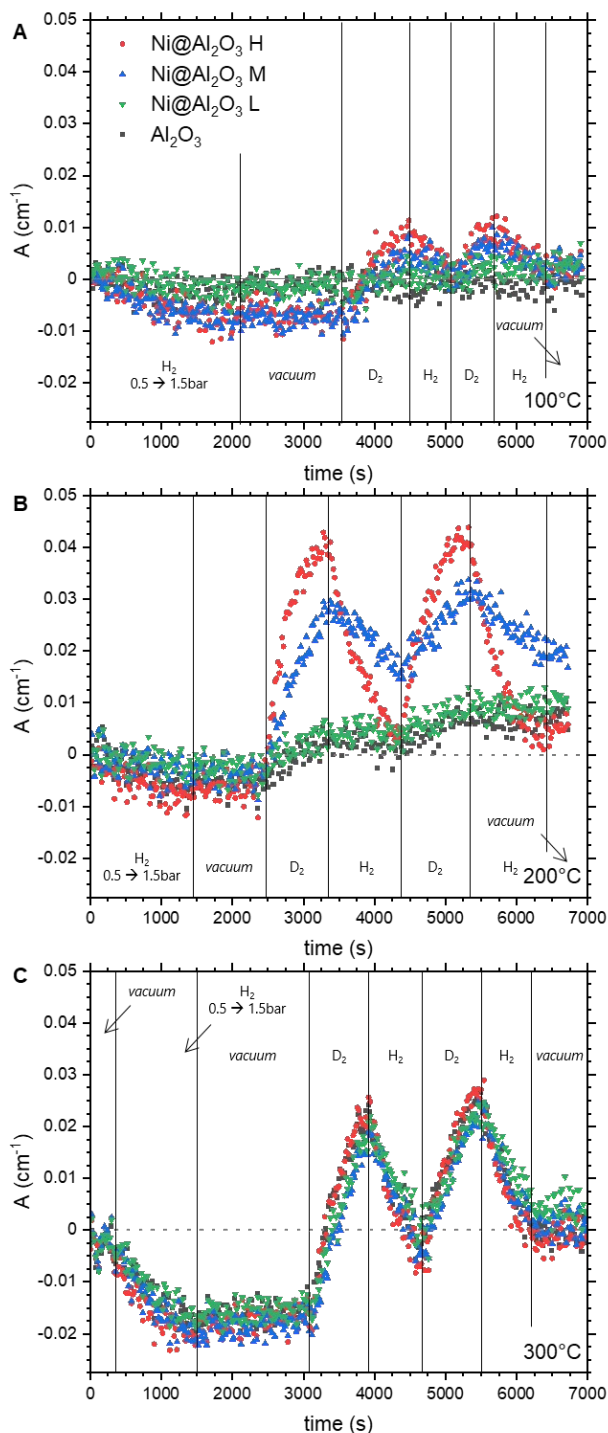


Fig. 5 A., B., and C. shows the neutron attenuation during hydrogenation and hydrogen–deuterium exchange versus time of various Ni@Al<sub>2</sub>O<sub>3</sub> catalysts with different Ni loads and the pristine Al<sub>2</sub>O<sub>3</sub> support at 100 °C, 200 °C and 300 °C, respectively.

state NMR.<sup>60</sup> Giving the fact that the measurement procedure are very different, the agreement is reasonable.

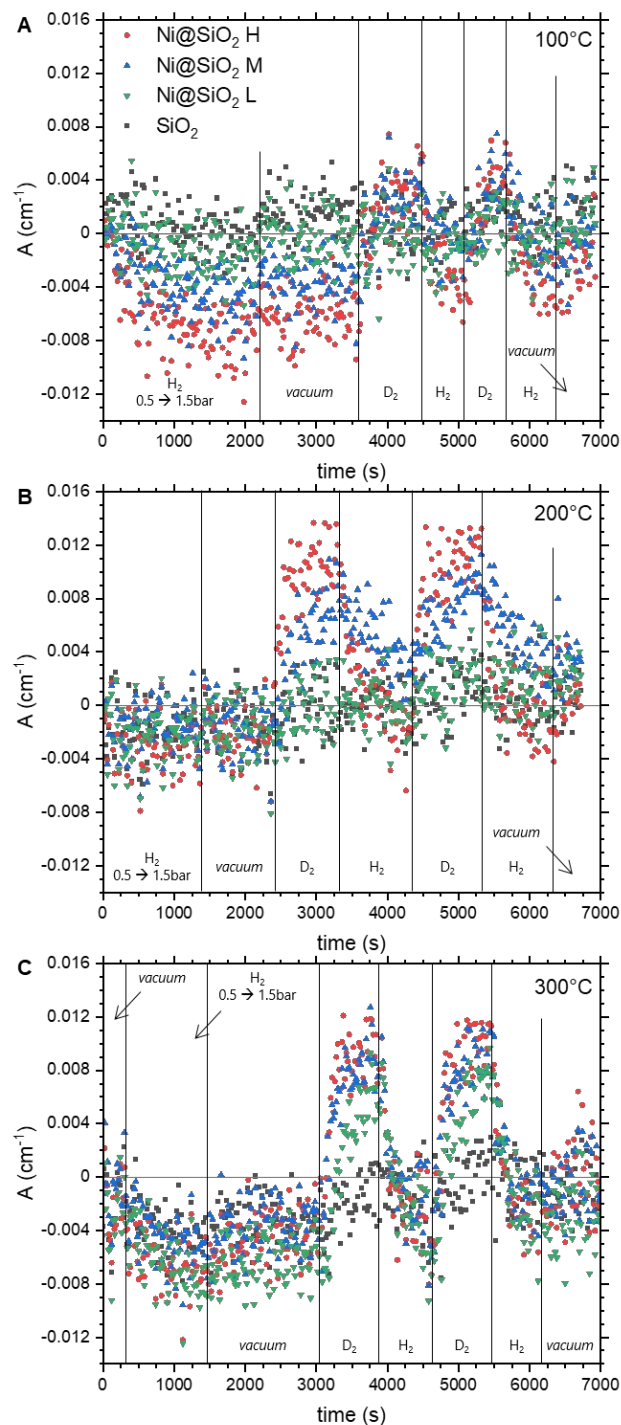


Fig. 6 A., B., and C. shows the neutron attenuation during hydrogenation and hydrogen–deuterium exchange versus time of various Ni@SiO<sub>2</sub> catalysts with different Ni loads and the pristine SiO<sub>2</sub> support at 100 °C, 200 °C and 300 °C, respectively.

The situation is different for Pt@WO<sub>3</sub>. Upon exposure to hydrogen during the first 1500 seconds, the initial attenuation drops

fast, and continues at a slower pace indicative of fast hydrogen uptake (red arrow in Fig. 4B). The hydrogen uptake is reversible: the attenuation weakens again fast and then slowly back to small absolute values when *vacuum* is applied (blue arrow in Fig. 4B). The final value differs to the initial one, which can be interpreted in two ways:

Hydrogen intercalates only partially into  $\text{WO}_3$  (Fig. 4C), and some hydrogen interacts irreversibly with the surface forming stable hydroxides and/or water; or the hydrogen intercalation (diffusion) into  $\text{WO}_3$  is time dependent, in particular at low hydrogen contents. For both scenarios, arguments can be found in literature.<sup>48,55,56,63–65</sup> By applying deuterium, we probe all kinetically accessible hydrogen in the sample, including the thermodynamically irreversibly absorbed hydrogen. The attenuation returns back to zero (violet arrow in Fig. 4B), and only a small positive attenuation develops (green arrow in Fig. 4B), which is indicative of (irreversibly absorbed) hydrogen that was present before first hydrogenation at  $t = 0$ .

Similar to Ni on  $\text{Al}_2\text{O}_3$ , the hydrogen concentration in  $\text{WO}_3$  is derived from the neutron attenuation. As we are interested in the bulk absorption of  $\text{H}_x\text{WO}_3$ , the number of hydrogen atom at 200 °C is given relative to the number of  $\text{WO}_3$ :

$$x = \frac{A}{\mu N_A} \cdot \frac{V_{\text{sample}} M_{\text{WO}_3}}{m_{\text{sample}}} \simeq 0.09 \text{ H per WO}_3 \quad (3)$$

The amount measured at 100 °C reached  $x = 0.26$  (not shown), which is in fair agreement with Berzins et al.<sup>55</sup> reporting  $x = 0.36$  and  $x = 0.20$  in  $\text{H}_x\text{WO}_3$  for 100 °C and 200 °C, respectively.

The hydrogen interaction with catalysts is very sensitive to temperature. The high-throughput method is ideal to study this dependency of a great number of samples in parallel reducing the unavoidable errors from experimental uncertainties, because the error is identical for all samples. As a demonstration, we studied the system Ni on  $\text{Al}_2\text{O}_3$  and Ni on  $\text{SiO}_2$  as a function of Ni load and temperature. Figure 5 shows the neutron attenuation during hydrogenation and hydrogen–deuterium exchange versus time of various Ni@ $\text{Al}_2\text{O}_3$  catalysts with different Ni loads and at various temperatures.

The 200 °C curve was already discussed above (Fig. 4). The results are similar for all investigated systems, i.e., a small reversible hydrogen uptake, and comparably larger irreversible hydrogen concentration. Not surprisingly, the catalysts with highest Ni loads have fastest kinetics (Fig. 5 & 7A). The temperature of maximum hydrogen–deuterium exchange rate is shown in Figure 7A. The kinetics were obtained by fitting the hydrogen–deuterium exchange for all samples with a linear equation for the first 200 s. The slope obtained in this way was then multiplied by the corresponding time to calculate the attenuation and the amount of exchanged hydrogen with deuterium, respectively. Interestingly, the differences are negligible at 300 °C, where hydrogen uptake as well as exchange is almost equally fast even on the pristine  $\text{Al}_2\text{O}_3$  support (Fig. 7A). Furthermore, the effect of Ni is significant only above a certain concentration (above a ratio of 0.3 Ni/Al, 0.03 Ni/Si respectively, Fig. 5 and Table 1) at lower temperatures. The Ni concentration as determined by XPS and

HAXPES (see experimental section) is an integral measure of the number (coverage) and size of Ni-particle on the oxide support. It is not expected that the catalytic activity for hydrogen–deuterium exchange of the Ni particles depend significantly on size. However, at very low concentrations and thus coverage, the diffusion length of H and or D is markedly larger than for high Ni concentrations. Karim et al.<sup>26</sup> find maximum diffusion lengths of 15 nm on  $\text{Al}_2\text{O}_3$ , i.e., the effect of a catalyst on hydrogen spillover is very local in perfect agreement with our results. Karim et al. substantiate the limited diffusion length with DFT-calculations finding that hydrogen desorbs during surface diffusion. This implies that this surface hydrogen is reversible. Indeed, we find the amount of reversible hydrogen (i.e., hydrogen adsorbed during hydrogenation) increases with temperature, while the amount of irreversibly adsorbed hydrogen (i.e., hydrogen–deuterium exchange) first increases (kinetics) and then decreases again at high temperature for the catalyst with highest Ni load (Fig. 5) and thus fastest kinetics. Following the argument of Joubert et al., hydrogen adsorption on Alumina is fully reversible at 400 °C.<sup>60</sup>

Hydrogen adsorption on  $\text{Al}_2\text{O}_3$  is known to be special, in particular the existence of hydrogen linked to Al with acidic character. The number of these 'acidic sites' are much smaller on silica than on alumina.<sup>38,66–69</sup> making Ni@ $\text{SiO}_2$  a good system for comparison. The amount of Ni on the catalyst surface of  $\text{SiO}_2$  is smaller by one order of magnitude compared to the  $\text{Al}_2\text{O}_3$  catalysts, even though the same amount of nickel precursor was used (table 1).<sup>38,39</sup> Figure 6 shows the neutron attenuation during hydrogenation and hydrogen–deuterium exchange versus time of various Ni@ $\text{SiO}_2$  catalysts with different Ni loads and at various temperatures.

The number of adsorbed and exchanged hydrogen is markedly smaller on Ni@ $\text{SiO}_2$  than on Ni@ $\text{Al}_2\text{O}_3$ , thus leading to more noisy neutron attenuation data. Using eq. 2 and a BET surface area of  $A_{\text{BET}} = 173.1 \text{ m}^2\text{g}^{-1}$ , the mass  $m = 0.112 \text{ g}$  and a neutron attenuation of  $A = 0.012 \text{ cm}^{-1}$ , we obtain an irreversibly bound hydrogen concentration of around  $2.2 \text{ H nm}^{-2}$  for Ni@ $\text{SiO}_2$  H at 300 °C (see Fig. 6). Chronister et al. report values between 1 and  $2 \text{ H nm}^{-2}$  using pyridine adsorption.<sup>67</sup>

Overall the Ni on  $\text{SiO}_2$  impregnated catalysts show a similar trend compared to the alumina catalysts. The amount of reversible hydrogen (i.e., hydrogen adsorbed during hydrogenation) increases with temperature. The amount of irreversibly adsorbed hydrogen (i.e., hydrogen–deuterium exchange) first increases, i.e., the adsorption is limited by kinetics. At high temperatures, the Ni loading becomes less relevant for the uptake (Fig. 6), while the rate still depends on the Ni loading (Fig. 7B). This means that at higher temperature, also the desorption is increased and thus the irreversibly adsorbed hydrogen decreases again.

## 5 Discussion

We introduced a quantitative method to monitor the H-uptake and hydrogen–deuterium exchange in materials, in particular catalysts. A particular strength of the method is that it gives quantitative data without needing a reference sample, which is indeed confirmed by comparison with literature data based on different

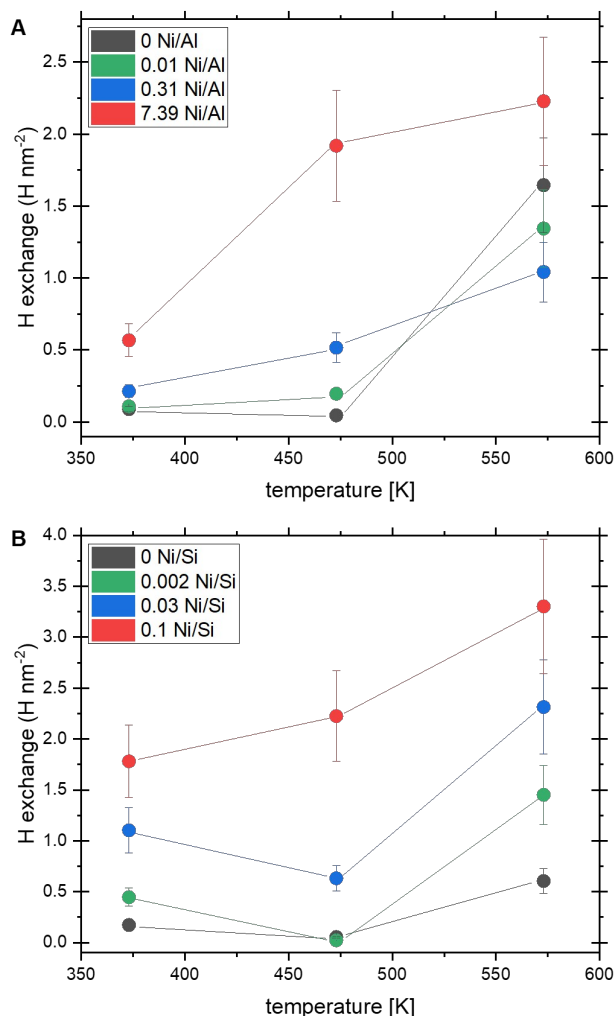


Fig. 7 A. and B. show the hydrogen–deuterium exchange after 200 seconds of applying deuterium on Ni catalysts supported by  $\text{Al}_2\text{O}_3$  (A.) and  $\text{SiO}_2$  (B.), respectively. The amount of Ni is given as metal to support cation ratios obtained by XPS analysis (from Table 1).

methods. However, there are limitations to this approach:

- signal to noise ratio: The final result, i.e., the hydrogen (OH) coverage in  $\text{Al}_2\text{O}_3$  and  $\text{SiO}_2$  supported catalysts is similar, but the underlying signal-to-noise ratios vary markedly (compare scattering of A in Figs. 5 and 6). The difference is due to different total amounts of hydrogen as a result of the total amount of the sample and its hydrogen content. The neutron attenuation is proportional to the number of hydrogen atoms, an extensive property, and not to the coverage or concentration, which is an intensive one. The signal to noise ratio can thus be enhanced by increasing the sample amount (attenuation length  $d$ ) until the total intensity is too low to be detected.
- cross section  $\mu$ : Equation 1 contains only experimental parameters, except  $\mu$ , which is approximated to be constant. This is based on the assumption that neutrons are atten-

uated by nuclear interaction with protons. However, the chemical bonding of the hydrogen with its environment influences the scattering cross section.<sup>70</sup> For the free hydrogen molecule,  $\mu_{\text{H}_2} = 3.7 \cdot 10^{-23} \text{ cm}^2$  per H,<sup>27</sup> while  $\mu_{\text{H}_2} = 4.0 \cdot 10^{-23} \text{ cm}^2$  per H,<sup>27,71</sup> for hydrogen in  $\text{ZrH}_x$ . We chose  $\mu_{\text{H}_2\text{O}} = 4.7 \cdot 10^{-23} \text{ cm}^2$ <sup>27,42</sup> assuming hydrogen in  $\text{H}_2\text{O}$  to be similar to hydrogen in OH. Without additional energy discrimination, CONI being based on an interaction between neutrons and nuclei cannot distinguish between atomic hydrogen, hydride ion or proton.

With the combinatorial approach of CONI considering all known different physical parameters of the individual samples, we can conclude on the chemical behavior of the studied systems:

- $\text{WO}_3$  is one of the best known examples of the hydrogen spillover effect. The oxide is reduced by hydrogen when it comes into contact with a metal catalyst (here Pt). Reduction can mean hydrogen intercalation forming  $\text{H}_x\text{WO}_3$ ,<sup>55</sup> adsorption at the surface and formation of hydroxy groups at surface,<sup>72,73</sup> and oxygen removal by water formation leading to oxygen deficient  $\text{WO}_{3-\delta}$ .<sup>48,74</sup> The latter takes place at higher temperatures only, and can thus be omitted here.<sup>55</sup> The competition between irreversible surface adsorption and reversible bulk absorption is debated since long.<sup>55,56,72,73</sup> CONI is ideal to distinguish the two processes (Fig. 4B). Bulk absorption is characterized by the reversible hydrogen uptake (red/blue arrow), while the existence of irreversible hydroxy groups is evidenced by hydrogen–deuterium exchange (green arrow).
- $\text{Al}_2\text{O}_3$  and  $\text{SiO}_2$  are archetypal catalyst support materials. Here, hydrogen interaction is supposed to take place on the surface, which is indeed observed by CONI. Both catalyst supports are non-reducible and therefore less susceptible to hydrogen spillover, i.e., only negligible net atomic hydrogen transport from the metal particle to the support surface.<sup>26,45</sup> The most common form of hydrogen transport on non-reducible supports is a proton–deuteron exchange of irreversible hydrogen, i.e., no additional hydrogen/deuterium absorption occurs on the catalyst/support surface (see figures 5 & 6). However, if alumina and silica are treated and evacuated at higher temperatures, defect sites are released which can then absorb atomic hydrogen, i.e. experience  $\text{H}_2$  spillover (see figures 5C & 6C).<sup>45,51,60</sup> Alumina in particular has relatively strong Lewis acid sites (aluminum elements that are not fully coordinated) that can be activated during treatment at elevated temperatures.<sup>51,60,75</sup> These activated sites can carry out hydrogenation reactions.<sup>76,77</sup> Our finding of absorbed hydrogen on  $\text{Al}_2\text{O}_3$  (Fig. 5) after evacuation at elevated temperatures differs not only by the observed amount of absorbed hydrogen (see results), but also by the fact that the hydrogen–deuterium exchange is temperature dependent, i.e. occurs only at higher temperatures, from the findings of Joubert et al.<sup>60</sup> and Wischert et al.<sup>51</sup> The amount of hydrogen–deuterium exchange increased with temperature for the pristine  $\text{Al}_2\text{O}_3$  support. At 100 °C hardly any

hydrogen–deuterium exchange was observed on the pristine  $\text{Al}_2\text{O}_3$  support, where as at 300 °C the exchange was equal to the Ni impregnated catalysts. Several aspects could be assigned for the difference in the findings, e.g. the signal-to-noise ratio, the starting materials and their preparation. Since the signal-to-noise ratio was relatively high for the  $\text{Al}_2\text{O}_3$  samples (Fig. 5), the latter can be considered as the cause of the difference. The nature of the starting materials (i.e., fumed silica, base-activated alumina) may also have contributed to the fact that the alumina catalysts were impregnated with much more nickel (Table 1). However, it can be assumed that the impregnation had no effect on the support structure, as observed in the XRD (Fig. 3).

Overall the determination of the total OH concentration with neutron radiography, yielded concentrations in good agreement with literature. The temperature dependence of the H intercalation and hydrogen–deuterium exchange show that an increased nickel content accelerates hydrogen–deuterium exchange, especially at lower temperatures. In addition, it is also evident that although the exchange rate of H/D increases at the highest temperatures (Fig. 7), the total amount absorbed is much smaller compared to lower temperatures (see figures. 5, & 6. This can be attributed to hydrogen desorption from the surface, which increases with higher temperatures.<sup>26</sup>

Spillover is dissociation of dihydrogen on the metal particle and the net transport of hydrogen over the surface of the support.<sup>45</sup> This is to be distinguished from hydrogen–deuterium exchange on hydrogen covered surfaces (e.g., in the form of OH). Here, the metal particle splits hydrogen/deuterium and thereby enables H/D-exchange, but there is no net transport over the surface, i.e., there is no additional hydrogen–deuterium adsorption (i.e., an local exchange of a proton with a deuteron). The neutron imaging visualizes these two effects (see, e.g., Fig. 5 C). The attenuation of neutrons increases upon hydrogen exposure indicative of hydrogen uptake. The reversibility is partially observed in  $\text{H@WO}_3$  (red/blue arrow in Fig. 4B), but hardly in  $\text{H@Al}_2\text{O}_3$  (Fig. 5C). The H/D-exchange process is reversible, but it relies on already existing hydrogen on the surface. In most cases, the hydrogen was already existing and is thus irreversibly adsorbed hydrogen such as OH. Despite involvement of irreversibly adsorbed hydrogen, hydrogen–deuterium exchange is very fast in contrast to spillover: for spillover, a net transport with correspondingly longer diffusion paths is needed, while hydrogen–deuterium exchange requires only local exchange.<sup>45</sup>

## 6 Conclusion and outlook

In this paper we utilize neutron imaging together with a combinatorial reactor (CONI method) as a valuable tool to characterize and probe the catalytic properties of up to 69 samples simultaneously, i.e., under identical reaction conditions. Overcoming the pressure gap we obtain more reliable catalyst properties closer to the industrially used conditions. The importance of the composition of the catalyst system (i.e., metal nanoparticles, metal loading, support) are well demonstrated. The use of neutrons

and the prior knowledge of the catalytic system allow to quantify the amount of and to distinguish between hydrogen adsorption/uptake, intercalation and exchange with deuterium. The presented case study of the Ni catalysts shows a clear dependence between the nickel content and the hydrogen exchange rate, especially at lower temperatures.

Future goal is to compare and correlate the measured neutron data with the catalytic reactions measured separately. This will contribute to the debated question,<sup>45</sup> to what extent spillover determines the activity of a catalyst for a given hydrogenation reaction.

## Author Contributions

**Marin Nikolic:** Conception of experiments, Experimental work, data evaluation, writing of manuscript. **Filippo Longo:** experimental work (neutron imaging, XPS/HAXPES measurements), data evaluation (XPS/HAXPES measurements). **Alessia Cesarini:** experimental work (neutron imaging,  $\text{N}_2$  sorption), data evaluation ( $\text{N}_2$  sorption). **Emanuel Billeter:** experimental work (neutron imaging). **Pavel Trtik:** neutron imaging experimental support, data evaluation (neutron imaging). **Andreas Borgschulte:** Conception of experiments, experimental work (neutron imaging), data evaluation, writing of manuscript. All authors have given approval to the final version of the manuscript.

## Conflicts of interest

The authors declare no conflicts of interest.

## Acknowledgements

The authors gratefully acknowledge financial support for the mega-move project from the ETHBoard (Board of the Swiss Federal Institutes of Technology). Additional funding via the UZH-UFSP program LightChEC and from the Swiss National Science Foundation [Grant no. 172662] was received.

## References

- 1 *High-Throughput Screening in Heterogeneous Catalysis*, ed. A. Hagmeyer, P. Strasser and A. F. Volpe, Wiley, 2004.
- 2 W. F. Maier, *Applied Catalysis A: General*, 2003, **254**, 1–170.
- 3 C. Allen, D. Leitch and M. e. a. Anson, *Nat. Catal.*, 2019, **2**, 2–4.
- 4 X. Liu, B. Liu, J. Ding, Y. Deng, X. Han, C. Zhong and W. Hu, *Advanced Functional Materials*, 2022, **32**, 2107862.
- 5 C. Ortega, D. Otyuskaya, E.-J. Ras, L. D. Virla, G. S. Patience and H. Dathe, *The Canadian Journal of Chemical Engineering*, 2021, **99**, 1288–1306.
- 6 F. C. Moates, M. Somani, J. Annamalai, J. T. Richardson, D. Luss and R. C. Willson, *Industrial & Engineering Chemistry Research*, 1996, **35**, 4801–4803.
- 7 H. Su and E. S. Yeung, *Journal of the American Chemical Society*, 2000, **122**, 7422–7423.
- 8 H. Su, Y. Hou, R. S. Houk, G. L. Schrader and E. S. Yeung, *Analytical Chemistry*, 2001, **73**, 4434–4440.
- 9 H. Su and E. S. Yeung, *Applied Spectroscopy*, 2002, **56**, 1044–1047.

- 10 M. Götz, J. Lefebvre, F. Mörs, A. McDaniel Koch, F. Graf, S. Bajohr, R. Reimert and T. Kolb, *Renewable Energy*, 2016, **85**, 1371–1390.
- 11 G. Centi and S. Perathoner, *Green Carbon Dioxide*, John Wiley & Sons, Inc., Hoboken, NJ, USA, 2014.
- 12 G. Schaub, H. Eilers and M. I. González, *Transition to Renewable Energy Systems*, 2013, pp. 619–628.
- 13 M. Iglesias G., C. de Vries, M. Claeys and G. Schaub, *Catalysis Today*, 2015, **242**, 184–192.
- 14 I. Chorkendorff and J. W. Niemantsverdriet, *Concepts of Modern Catalysis and Kinetics*, Wiley, 2003.
- 15 R. Schäppi, D. Rutz, F. Dähler, A. Muroyama, P. Haueter, J. Lilliestam, A. Patt, P. Furler and A. Steinfeld, *Nature*, 2022, **601**, 63–68.
- 16 P. Strucks, L. Failing and S. Kaluza, *Chemie Ingenieur Technik*, 2021, **93**, 1526–1536.
- 17 P. Sabatier and J. Senderens, *C. R. Acad. Sci.*, 1902, **134**, 689–691.
- 18 P. Sabatier and J. Senderens, *C. R. Acad. Sci.*, 1902, **134**, 514–516.
- 19 M. Saito, T. Fujitani, M. Takeuchi and T. Watanabe, *Applied Catalysis A: General*, 1996, **138**, 311–318.
- 20 K. Klier, *Methanol Synthesis*, 1982, pp. 243–313.
- 21 K. Waugh, *Catalysis Today*, 1992, **15**, 51–75.
- 22 Y. Song, Y. He and S. Laursen, *Catal. Sci. Technol.*, 2022, **12**, 3568–3581.
- 23 M. D. Porosoff, B. Yan and J. G. Chen, *Energy & Environmental Science*, 2016, **9**, 62–73.
- 24 F. M. Pinto, V. Y. Suzuki, R. C. Silva and F. A. La Porta, *Frontiers in Materials*, 2019, **6**.
- 25 C. Pirola, F. Galli and G. S. Patience, *The Canadian Journal of Chemical Engineering*, 2018, **96**, 2317–2320.
- 26 W. Karim, C. Spreafico, A. Kleibert, J. Gobrecht, J. VandeVondele, Y. Ekinici and J. A. van Bokhoven, *Nature*, 2017, **541**, 68–71.
- 27 E. Lehmann, P. Vontobel and N. Kardjilov, *Applied Radiation and Isotopes*, 2004, **61**, 503–509.
- 28 P. C. H. Mitchell, S. F. Parker, A. J. Ramirez-Cuesta and J. Tomkinson, *Vibrational Spectroscopy with Neutrons*, WORLD SCIENTIFIC, 2005, vol. 3.
- 29 S. F. Parker and D. Lennon, *Physchem*, 2021, **1**, 95–120.
- 30 N. Kardjilov, I. Manke, A. Hilger, M. Strobl and J. Banhart, *Materials Today*, 2011, **14**, 248–256.
- 31 A. Borgschulte, R. Delmelle, R. B. Duarte, A. Heel, P. Boillat and E. Lehmann, *Physical Chemistry Chemical Physics*, 2016, **18**, 17217–17223.
- 32 J. Terreni, E. Billeter, O. Sambalova, X. Liu, M. Trottmann, A. Sterzi, H. Geerlings, P. Trtik, A. Kaestner and A. Borgschulte, *Phys. Chem. Chem. Phys.*, 2020, **22**, 22979–22988.
- 33 D. Hu, J. Gao, Y. Ping, L. Jia, P. Gunawan, Z. Zhong, G. Xu, F. Gu and F. Su, *Industrial & Engineering Chemistry Research*, 2012, **51**, 4875–4886.
- 34 R.-P. Ye, W. Gong, Z. Sun, Q. Sheng, X. Shi, T. Wang, Y. Yao, J. J. Razink, L. Lin, Z. Zhou, H. Adidharma, J. Tang, M. Fan and Y.-G. Yao, *Energy*, 2019, **188**, 116059.
- 35 K. Hadjiivanov, P. Lukinskas and H. Knözinger, *Catalysis Letters*, 2002, **82**, 73–77.
- 36 O. Sambalova, E. Billeter, J. Mann, T. Miyayama, D. Burnat, A. Heel, D. Bleiner and A. Borgschulte, *Surface and Interface Analysis*, 2020, **52**, 811–817.
- 37 H. Shinotsuka, S. Tanuma, C. J. Powell and D. R. Penn, *Surface and Interface Analysis*, 2015, **47**, 871–888.
- 38 P. Munnik, P. E. de Jongh and K. P. de Jong, *Chemical Reviews*, 2015, **115**, 6687–6718.
- 39 L. Bonneviot, M. Che, D. Olivier, G. A. Martin and E. Freund, *The Journal of Physical Chemistry*, 1986, **90**, 2112–2117.
- 40 E. H. Lehmann, P. Vontobel and L. Wiezel, *Nondestructive Testing and Evaluation*, 2001, **16**, 191–202.
- 41 B. Blau, K. N. Clausen, S. Gvasaliya, M. Janoschek, S. Janssen, L. Keller, B. Roessli, J. Schefer, P. Tregenna-Piggott, W. Wagner and O. Zaharko, *Neutron News*, 2009, **20**, 5–8.
- 42 D. Mannes, L. Josic, E. Lehmann and P. Niemz, *Holzforschung*, 2009, **63**, 472–478.
- 43 C. Carminati, P. Boillat, F. Schmid, P. Vontobel, J. Hovind, M. Morgano, M. Raventos, M. Siegwart, D. Mannes, C. Gruenzweig, P. Trtik, E. Lehmann, M. Strobl and A. Kaestner, *PLOS ONE*, 2019, **14**, e0210300.
- 44 K. Christmann, *Surface Science Reports*, 1988, **9**, 1–163.
- 45 R. Prins, *Chemical Reviews*, 2012, **112**, 2714–2738.
- 46 Y. Fukai, *The Metal-Hydrogen System*, Springer Berlin Heidelberg, Berlin, Heidelberg, 1993, vol. 21.
- 47 A. Borgschulte, J. Terreni, B. Fumey, O. Sambalova and E. Billeter, *Frontiers in Energy Research*, 2022, **9**.
- 48 E. Billeter, A. Sterzi, O. Sambalova, R. Wick-Joliat, C. Grazioli, M. Coreno, Y. Cheng, A. J. Ramirez-Cuesta and A. Borgschulte, *Phys. Rev. B*, 2021, **103**, 205304.
- 49 T. Y. Wei, K. Lim, Y. S. Tsenga and S. L. I. Chan, *Renew. Sustain. Energy Rev.*, 2017, **79**, 1122–113383.
- 50 J. Terreni, M. Trottmann, R. Delmelle, A. Heel, P. Trtik, E. H. Lehmann and A. Borgschulte, *The Journal of Physical Chemistry C*, 2018, **122**, 23574–23581.
- 51 R. Wischert, C. Copéret, F. Delbecq and P. Sautet, *Angewandte Chemie International Edition*, 2011, **50**, 3202–3205.
- 52 J. E. S. van der Hoeven, H. T. Ngan, A. Taylor, N. M. Eagan, J. Aizenberg, P. Sautet, R. J. Madix and C. M. Friend, *ACS Catalysis*, 2021, **11**, 6971–6981.
- 53 A. Borgschulte, M. Biemann, A. Züttel, G. Barkhordarian, M. Dornheim and R. Bormann, *Applied Surface Science*, 2008, **254**, 2377–2384.
- 54 F. Wöhler, *Ann. Phys.*, 1824, **78**, 345–358.
- 55 A. R. Berzins and P. A. Sermon, *Nature*, 1983, **303**, 506–508.
- 56 M. F. Saenger, T. Höing, B. W. Robertson, R. B. Billa, T. Hofmann, E. Schubert and M. Schubert, *Phys. Rev. B*, 2008, **78**, 245205.
- 57 A. P. Amrute, Z. Łodziana, H. Schreyer, C. Weidenthaler and F. Schüth, *Science*, 2019, **366**, 485–489.
- 58 Y. Wang, G. K. Pálsson, H. Raanaei and B. Hjörvarsson, *Jour-*

- nal of Alloys and Compounds*, 2008, **464**, L13–L16.
- 59 J. M. Schneider, A. Anders, B. Hjörvarsson, I. Petrov, K. Macák, U. Helmersson and J.-E. Sundgren, *Applied Physics Letters*, 1999, **74**, 200–202.
- 60 J. Joubert, A. Salameh, V. Krakoviack, F. Delbecq, P. Sautet, C. Copéret and J. M. Basset, *The Journal of Physical Chemistry B*, 2006, **110**, 23944–23950.
- 61 J. Terreni, O. Sambalova, A. Borgschulte, S. Rudić, S. F. Parker and A. J. Ramirez-Cuesta, *Catalysts*, 2020, **10**,.
- 62 W. Zhang, M. Sun and R. Prins, *The Journal of Physical Chemistry B*, 2002, **106**, 11805–11809.
- 63 M. A. Vannice, M. Boudart and J. J. Fripiat, *J. Catal.*, 1970, **17**, 359–365.
- 64 M. Vasilopoulou, I. Kostis, N. Vourdas, G. Papadimitropoulos, A. Douvas, N. Boukos, S. Kennou and D. Davazoglou, *The Journal of Physical Chemistry C*, 2014, **118**, 12632–12641.
- 65 E. Lalik, K. Družbicki, G. Irvine, M. Gutmann, S. Rudić, P. Manuel, V. Petříček and M. Krzystyniak, *The Journal of Physical Chemistry C*, 2021, **125**, 23864–23879.
- 66 P. Hobza, J. Sauer, C. Morgeneyer, J. Hurych and R. Zahrádník, *The Journal of Physical Chemistry*, 1981, **85**, 4061–4067.
- 67 C. W. Chronister and R. S. Drago, *Journal of the American Chemical Society*, 1993, **115**, 4793–4798.
- 68 P. Ugliengo, A. M. Ferrari, A. Zecchina and E. Garrone, *The Journal of Physical Chemistry*, 1996, **100**, 3632–3645.
- 69 W. Yang, Z. Wang, J. Huang and Y. Jiang, *The Journal of Physical Chemistry C*, 2021, **125**, 10179–10197.
- 70 W. L. Whittemore and A. W. McReynolds, *Phys. Rev.*, 1959, **113**, 806–808.
- 71 M. Grosse, E. Lehmann, P. Vontobel and M. Steinbrueck, *Nuclear Instruments and Methods in Physics Research Section A: Accelerators, Spectrometers, Detectors and Associated Equipment*, 2006, **566**, 739–745.
- 72 A. Antonaia, M. Santoro, G. Fameli and T. Polichetti., *Thin Solid Films*, 2003, **426**, 281–287.
- 73 M. Daniel, B. Desbat, J. Lassegues, B. Gerand and M. Figlarz, *Journal of Solid State Chemistry*, 1987, **67**, 235–247.
- 74 W. Wang, A. Janotti and C. G. Van de Walle, *J. Mater. Chem. C*, 2016, **4**, 6641–6648.
- 75 E. Parry, *Journal of Catalysis*, 1963, **2**, 371–379.
- 76 Y. Amenomiya, J. Chenier and R. Cvetanovic, *Journal of Catalysis*, 1967, **9**, 28–37.
- 77 V. K. Rajagopal, R. D. Guthrie, T. Fields and B. H. Davis, *Catalysis Today*, 1996, **31**, 57–63.